



PERGAMON

International Journal of Impact Engineering 23 (1999) 723–734

www.elsevier.com/locate/ijimpeng

INTERNATIONAL
JOURNAL OF
**IMPACT
ENGINEERING**

PENETRATION OF 6061-T6511 ALUMINUM TARGETS BY OGIVE-NOSE STEEL PROJECTILES WITH STRIKING VELOCITIES BETWEEN 0.5 AND 3.0 KM/S

ANDREW J. PIEKUTOWSKI*, MICHAEL J. FORRESTAL**,
KEVIN L. POORMON*, and THOMAS L. WARREN**

*University of Dayton Research Institute, 300 College Park Avenue, Dayton, OH 45469-0182, USA

**Sandia National Laboratories, Albuquerque, NM 87185-0315, USA

Summary—We performed a series of depth-of-penetration experiments using 7.11-mm-diameter, 71.12-mm-long, ogive-nose steel projectiles and 254-mm-diameter, 6061-T6511 aluminum targets. The projectiles were made from vacuum-arc remelted (VAR) 4340 steel (R_c 38) and AerMet 100 steel (R_c 53), had a nominal mass of 0.021 kg, and were launched using a powder gun or a two-stage, light gas gun to striking velocities between 0.5 and 3.0 km/s. Since the tensile yield strength of AerMet 100 (R_c 53) steel is about 1.5 times greater than VAR 4340 (R_c 38) steel, we were able to demonstrate the effect of projectile strength on ballistic performance. Post-test radiographs of the targets showed three different regions of penetrator response as the striking velocity increased: (1) the projectiles remained rigid and visibly undeformed; (2) the projectiles deformed during penetration without nose erosion, deviated from the target centerline, and exited the side of the target or turned severely within the target; and (3) the projectiles eroded during penetration and lost mass. To show the effect of projectile strength, we present depth-of-penetration data as a function of striking velocity for both types of steel projectiles at striking velocities ranging from 0.5 and 3.0 km/s. In addition, we show good agreement between the rigid-projectile penetration data and a cavity-expansion model. © 1999 Elsevier Science Ltd. All rights reserved.

INTRODUCTION

Most studies of the penetration of long-rod projectiles launched with high striking velocities have focused on tungsten projectiles impacting steel [1, 2] or confined ceramic [3] targets. Silsby [1] conducted experiments with tungsten alloy long rods and armor steel targets at striking velocities between 1.3 and 4.5 km/s. For those experiments, depth of penetration increased monotonically and eventually reached a limiting depth as striking velocity increased. Anderson *et al.* [2] present data from [1] and five other studies for tungsten rod projectiles with length-to-diameter ratios of 20. When the penetration-depth data were divided by the rod length and plotted versus striking velocity, all six data sets showed small scatter in the normalized plot. This same relationship between penetration depth and striking velocity was reported recently by Orphal *et al.* [3] for confined ceramic targets. For highly resistive steel and confined ceramic targets, the projectile deforms at impact and erodes during the penetration process.

In contrast, penetration experiments that used T-200 maraging steel [4], long-rod projectiles with a 3.0 caliber-radius-head (CRH) nose shape and 6061-T651 aluminum targets [5] showed that the projectiles were visibly undeformed for striking velocities up to 1.46 km/s. For higher striking velocities, post-test radiographs of the targets showed that the projectile shanks fractured into several segments in the penetration channel or cavity. Penetration experiments with the same maraging steel projectiles and 7075-T651 aluminum targets [6] showed that the projectiles

remained visibly undeformed for striking velocities up to 1.26 km/s and fractured in the penetration channel for higher striking velocities. For both of these studies [5 and 6], the depth of penetration increased with striking velocity until the projectile fractured. For the 6061-T651 aluminum targets [5], the maximum normalized penetration depth (penetration depth divided by the rod length) was 4.0. For aluminum targets and steel projectiles, jet theory predicts a normalized penetration depth of 1.7.

In this study, we performed two series of penetration experiments with ogive-nose, steel, long-rod projectiles and 6061-T6511 aluminum targets at striking velocities between 0.5 and 3.0 km/s. The studies were performed to observe the response regions from rigid-body penetration through eroding-rod penetration. To avoid projectile shank fracture, we used moderately hard, vacuum-arc remelted (VAR) 4340 steel projectiles for our first series of experiments. To show the effect of yield strength on ballistic performance, harder AerMet 100 steel projectiles were used for the second set of experiments. In the next sections, we describe our experiments and present our results. In addition, we modified our cavity-expansion penetration model, given in Refs. [5] and [7], to predict the rigid-body response of ogive-nose projectiles. The model showed good agreement with penetration depth data for striking velocities up to 1.8 km/s.

EXPERIMENTS

The dimensions of the ogive-nose, steel projectiles used in both series of penetration experiments are given in Fig. 1. The 6061-T6511 aluminum targets were 254 mm in diameter. The length of the target was determined to be the sum of the anticipated depth of penetration plus the length of the rod. The first series of experiments was performed using VAR 4340 steel [8] projectiles that had a hardness of R_C 38, a tensile yield strength of 1140 MPa (165 ksi), and a fracture toughness of 130 MPa (m)^{1/2} or 120 ksi (in.)^{1/2}. The second set of experiments used AerMet 100 steel [9, 10] projectiles that had a hardness of R_C 53, a tensile yield strength of 1720 MPa (250 ksi), and a fracture toughness of 126 MPa (m)^{1/2} or 115 ksi (in.)^{1/2}. Thus, both steel projectiles had nearly the same fracture toughness, but the AerMet 100 steel had 1.5 times the tensile yield strength as the VAR 4340 steel.

For striking velocities below 1.3 km/s, the projectiles were launched using a 20 mm powder gun. For striking velocities above 1.3 km/s, the projectiles were launched using a 50/20 mm or a 75/30 mm, two-stage, light-gas gun. Projectile striking velocities were measured with an accuracy of better than 0.5 percent using four laser-photodetector stations installed at various locations along the flight path. The pitch and yaw of the projectile was obtained from radiographs obtained with use of an orthogonal pair of flash x-rays positioned immediately in front of the face of the target. The depth of penetration of the projectile and the final shape of the projectile were determined, after each test, from a radiograph of a 38-mm-thick slice of the target. The slice was cut from each target with special care to ensure the plane of maximum inclination of the rod was

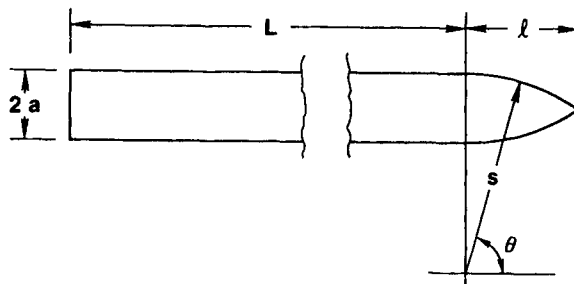


Fig. 1. Geometry for the ogive-nose rod with a 3.0 caliber-radius-head (CRH), $L = 59.3$ mm, $l = 11.8$ mm, and $2a = 7.11$ mm. Note that for a 3 CRH rod, $s = 3 \times 2a$.

coincident with the plane of the slice. Tables 1 and 2 summarize the penetration data from both series of experiments.

As shown in Table 1, we performed 20 experiments using VAR 4340 steel projectiles. The projectile striking velocities ranged from 0.57 to 2.99 km/s. Depth of penetration increased as striking velocity was increased to 1.40 km/s. For striking velocities below 1.24 km/s, the projectiles remained visibly undeformed and the penetration channels were straight; however, the penetration channels for striking velocities of 1.36 and 1.40 km/s (Shots 4-1829 and 4-1799) exhibited significant curvature and the projectiles were bent. At striking velocities of 1.49 and 1.57 km/s (Shots 4-1800 and 4-1810), the projectiles exited the side of the target. For striking velocities between 1.58 and 1.77 km/s (Shots 4-1801, 4-1831, and 4-1808), the projectiles were severely deformed during penetration, but remained in the target. Finally, for striking velocities between 2.0 and 3.0 km/s (Shots 4-1832, 4-1809, 8-0113, 4-1833, 8-0112, and 8-0104), the projectiles eroded.

Selected radiographs of targets from tests using VAR 4340 steel projectiles are presented in Fig. 2. The radiographs selected for presentation in Fig. 2 illustrate the following changes in

Table 1. Penetration data for VAR 4340, R_C 38, 3-CRH-nosed, steel rods

Targets were 254-mm-diameter bars of 6061-T6511 aluminum with lengths shown below.

For Pitch, D = Down and U = Up. For Yaw, R = Right and L = Left.

Shot Number	Striking Velocity, V_S , (m/s)	Penetration ^a , (mm)	Mass, (g)	Penetrator Hardness, R_C	Pitch, Degrees	Yaw, Degrees	Target Length, (m)
1-0415	569	58	20.38	38.2	0	0.25 R	0.127
4-1805	570	55	20.427	38.1	3.0 U	2.0 R	0.141
4-1806	679	72	20.412	38.1	1.0 U	0.25 L	0.140
4-1796	821	102	20.415	38.9	1.75 U	0.2 R	0.167
4-1797	966	140	20.415	38.0	0.25 U	0.75 R	0.229
1-0412	1147	190	20.41	38.3	---	---	0.248
4-1798	1237	224	20.379	38.0	1.5 U	1.25 R	0.267
4-1829	1365	249 (252)	20.824	39.2	1.75 D	0.75 L	0.343
4-1799	1396	249 (267)	20.418	38.0	2.5 U	0	0.289
4-1800	1493	277 ^b (303)	20.383	38.0	0.25 U	1.5 R	0.338
4-1810	1571	(216) ^c	20.480	38.2	1.1 U	0.6 R	0.292
4-1801	1585	105 ^d	20.414	38.0	2.0 U	4.5 L	0.363
4-1831	1648	109 ^d	20.437	37.7	1.5 D	0.25 R	0.267
4-1808	1770	142 ^d	20.444	37.9	1.0 U	0.5 R	0.244
4-1832	1977	123	20.456	39.5	0.25 D	1.25 R	0.216
4-1809	2166	124	20.432	37.9	4.5 U	3.0 R	0.235
8-0113	2193	126	20.423	38.4	0.75 U	5.0 R	0.244
4-1833	2204	121	20.452	39.4	1.5 U	0.25 R	0.216
8-0112	2570	144	20.367	38.2	0.75 U	6.0 R	0.243
8-0104	2988	147	20.390	38.9	0.4 U	1.3 L	0.305

^a Depth of penetration measured normal to the surface of the target to the *point* of the projectile. Values shown in parentheses are the lengths of the penetration channels when the channels were curved.

^b Projectile exited side of target at this depth below the target surface. Exit angle was 65 to 70 degrees to the shot-line axis and exit velocity was low. The nose of the rod remained sharply pointed.

^c Projectile exited side of target at a depth of 141 mm below the target surface. Exit angle was 90 degrees to the shot-line axis and exit velocity was estimated to be 950 m/s. The nose of the rod remained sharply pointed.

^d Rod appeared to "turn around" during crater formation (i.e., the tail of the rod was at the bottom of the crater and the point of the rod was nearer the mouth of the crater).

Table 2. Penetration data for AerMet 100, R_C 53, 3-CRH-nosed, steel rods

Targets were 254-mm-diameter bars of 6061-T6511 aluminum with lengths shown below.

For Pitch, D = Down and U = Up. For Yaw, R = Right and L = Left.

Shot Number	Striking	Penetration ^a , (mm)	Mass, (g)	Penetrator		Yaw, Degrees	Target Length, (m)
	Velocity, V_S , (m/s)			Hardness, R_C	Pitch, Degrees		
1-0426	794	103	20.908	52.9	0.25 U	1.25 L	0.154
1-0424	1076	160	20.89	53.1	3.5 U	1.5 R	0.230
1-0425	1255	229	20.906	53.1	1.5 U	0.75 L	0.277
4-1840	1348	254	20.914	53.2	1.75 U	2.75 R	0.349
4-1841	1538	332	20.889	53.8	0	2.5 R	0.406
4-1842	1654	389	20.873	53.4	1 U	0.5 L	0.406
4-1843	1786	452	20.912	53.0	1 U	0.25 R	0.470
8-0117	1816	(398) ^b	20.788	53.5	3.25 D	0.25 R	0.559
4-1844	1817	462	20.916	53.3	0.75 U	0	0.559
8-0118	1916	(281) ^c	20.880	53.0	2.25 D	1.75 L	0.559
8-0123	2042	185 ^d	20.959	53.3	2.5 D	1.5 L	0.254
8-0121	2438	168 ^d	20.872	53.0	4.5 D	1.75 L	0.305
8-0120	2493	168 ^d	20.868	53.5	7 D	2.75 L	0.305
8-0119	2963	172 ^d	20.912	53.1	3.5 D	2.75 L	0.305

^a Depth of penetration measured normal to the surface of the target to the *point* of the projectile. Values shown in parentheses are the lengths of the penetration channels when the channels were curved.

^b Projectile exited side of target at 283 mm below the target surface. Exit angle was 40 degrees to the shot-line axis and exit velocity is estimated at 600 m/s. Splintered rod fragments were recovered.

^c Projectile exited side of target at 232 mm below the target surface. Exit angle was 60–65 degrees to the shot-line axis and exit velocity is estimated at 1300 m/s. Splintered rod fragments were recovered.

^d Projectile broken into small fragments.

penetrator response as striking velocity is increased. In Fig. 2a, the penetration channel is straight and coincident with the centerline of the target and the projectile is not visibly deformed. In Fig. 2b, the crater is straight but at an angle to the target centerline; however, the rod is not visibly deformed. The penetration channel is curved and the rod slightly bent in the crater shown in Fig. 2c. In Fig. 2d, the projectile produced a sharply curved channel before exiting the side of the target. In the radiograph shown in Fig. 2e, it is evident that the projectile experienced a sequence of severe deformations and came to rest with the tail of the rod at the bottom of the crater and the nose of the rod nearer the mouth of the crater. (Additional details of the features observed in the crater produced by this test are presented later in this section.) In Fig. 2f, the crater shows evidence of the beginning of eroding-rod penetration. The crater shown in Fig. 2g exhibits the features typically associated with eroding-rod penetration. As shown in Table 1, all of the rods exhibited some inclination, at impact, of their centerline to the shot-line axis and the surface of the target. The trajectory followed by the rod during penetration of the target was in the plane that was determined by the inclination angle of the projectile. This behavior was noted for both types of steel rods.

Penetration data for 14 experiments using AerMet 100 projectiles are presented in Table 2. Striking velocities for these tests ranged from 0.79 to 2.96 km/s. Depth of penetration increased as striking velocity increased to 1.82 km/s. For striking velocities between 0.79 and 1.79 km/s, the penetration channels were straight and the projectiles were not visibly deformed. At striking velocities of 1.82 and 1.92 km/s (Shots 8-0117, 4-1844, and 8-0118), the penetration channels were curved. The projectiles exited the sides of the targets for Shots 8-0117 and 8-0118, but remained in the target for Shot 4-1844. As shown in Table 2, the inclination angles of the rods

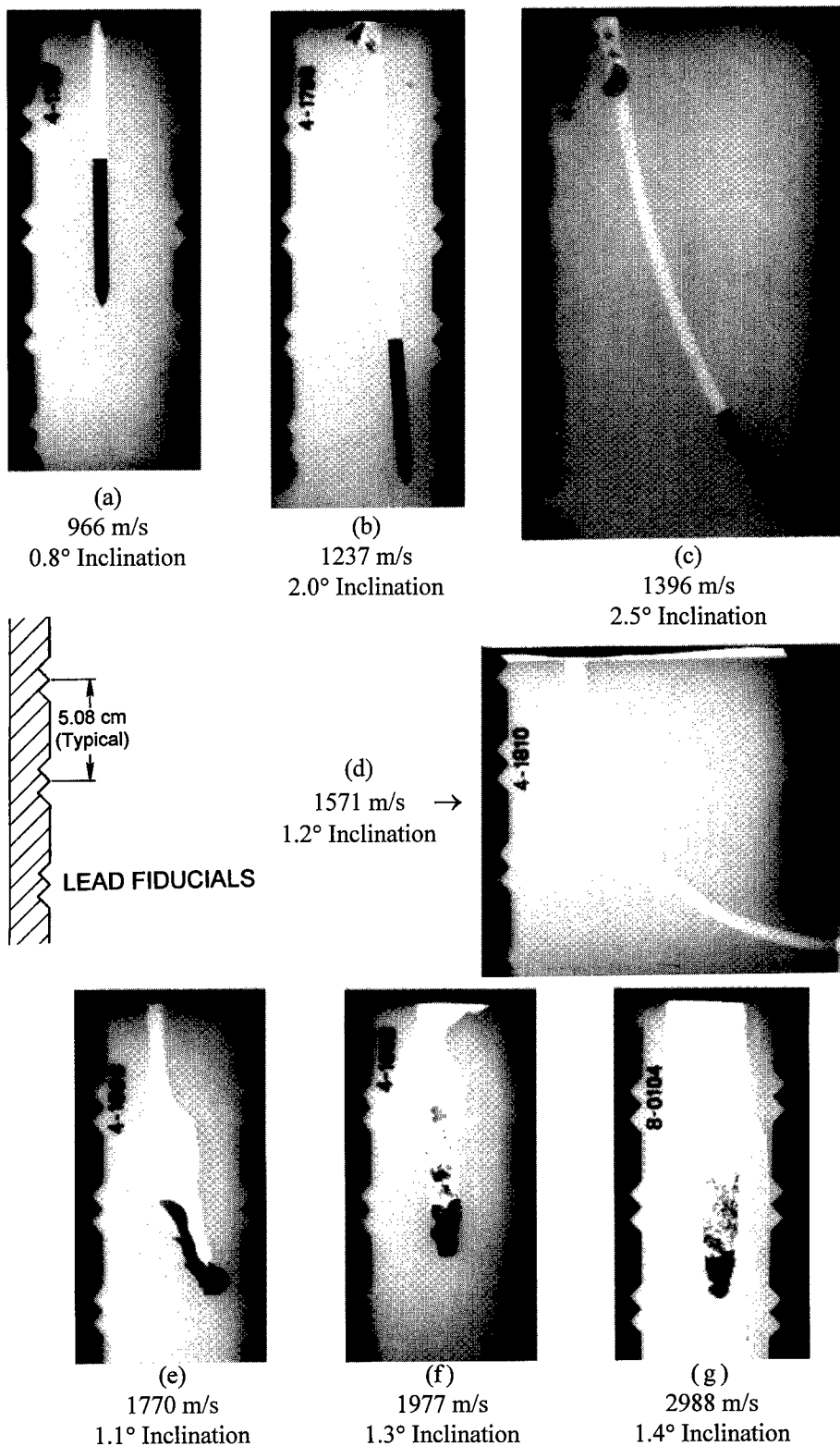


Fig. 2. Radiographs of craters produced by impact of ogive-nosed, VAR 4340 steel rods with 6061-T6511 aluminum targets. Striking velocity and the inclination angle of the rod at impact is noted below each crater.

for Shots 8-0117 and 8-0118 were higher than for the rod for Shot 4-1844. For striking velocities between 2.0 and 3.0 km/s (Shots 8-0123, 8-1021, 8-0120, and 8-0119), the projectiles broke into small fragments or eroded.

Selected radiographs of targets from tests using AerMet 100 steel projectiles are presented in Fig. 3. Again, the radiographs selected for presentation in Fig. 3 illustrate the changes in penetrator response as striking velocity is increased. In Fig. 3a, the penetration channel is straight, coincident with the centerline of the target, and the projectile is not visibly deformed. In Figs. 3b and 3c, the craters are straight but at an angle to the target centerline; however, the rods are not visibly deformed. The penetration channel shown in Fig. 3d is slightly curved and the rod exhibits a very slight bend. In Fig. 3e, the projectile produced a sharply curved channel before exiting the side of the target. In the radiograph shown in Fig. 3f, the projectile appears to have experienced severe deformation after entering the target. The right side of the crater profile for this shot exhibits two large “pouches” that may have been produced by severe bending and fracture of the front part of the rod during the early phase of the penetration event. The lower part of the crater exhibits features more typical of eroding-rod penetration. The crater shown in Fig. 3g exhibits the features usually associated with eroding-rod penetration.

The effect of projectile yield strength on the ability of an ogive-nose, long-rod to penetrate a semi-infinite target is shown in the target radiographs presented in Fig. 4. In this figure, the long, slightly curved penetration channel produced by the impact of an AerMet 100 steel rod is compared to the relatively short and uniquely shaped crater produced by the impact of a VAR 4340 steel rod. The initial conditions of striking velocity and inclination angle were nearly identical for both of the tests. The AerMet 100 steel rod penetrated as a rigid body. The VAR 4340 steel rod, on the other hand, appeared to penetrate normally for the first 40 mm or so and then began to turn sharply to the right. From an examination of the interior surface of the crater, it appears that the front end of the rod bent severely, formed a hook, and continued to penetrate the target. As noted in Fig. 4, the machined surface of the tail end of the rod is clearly evident in the sectioned target. A short section of the tail end of the rod is tightly curved but has broken from the front portion of the rod and is at the bottom of the crater. The nose and the remainder of the rod are pointing toward the mouth of the crater. Clearly, the rod turned around in a cavity that was less than three rod diameters wide while in the process of penetrating the target. More remarkably, the front portion of the rod appeared to straighten itself after it had turned around.

In the next section, we present our cavity-expansion, rigid-body, penetration model. We then compare depth-of-penetration-versus-striking-velocity data for the VAR 4340 and AerMet 100 steel projectiles with our model for the cases where the projectiles remained visibly undeformed.

RIGID-PROJECTILE PENETRATION MODEL

In this section, we present penetration equations for rigid, ogive-nose rods that penetrate 6061-T6511 aluminum targets at normal impact. This model uses the spherical cavity-expansion approximation [11] that closely simulates the two-dimensional target response with results from a dynamic, spherically symmetric cavity-expansion problem. In Ref. 7, Warren and Forrestal presented stress-strain data for 6061-T6511 aluminum at strain rates ranging from 10^{-3} s^{-1} to 10^5 s^{-1} and a constitutive equation that includes strain hardening and strain-rate sensitivity. Next, they solved the spherically symmetric, cavity-expansion problem and presented penetration equations for spherical-nose rods. We generalized the penetration equations for a spherical nose to that of an ogive nose with the procedures published in Refs. 5, 6, and 7.

For the 6061-T6511 targets and ogive-nose rod projectiles studied in this work, depth of penetration P is given by

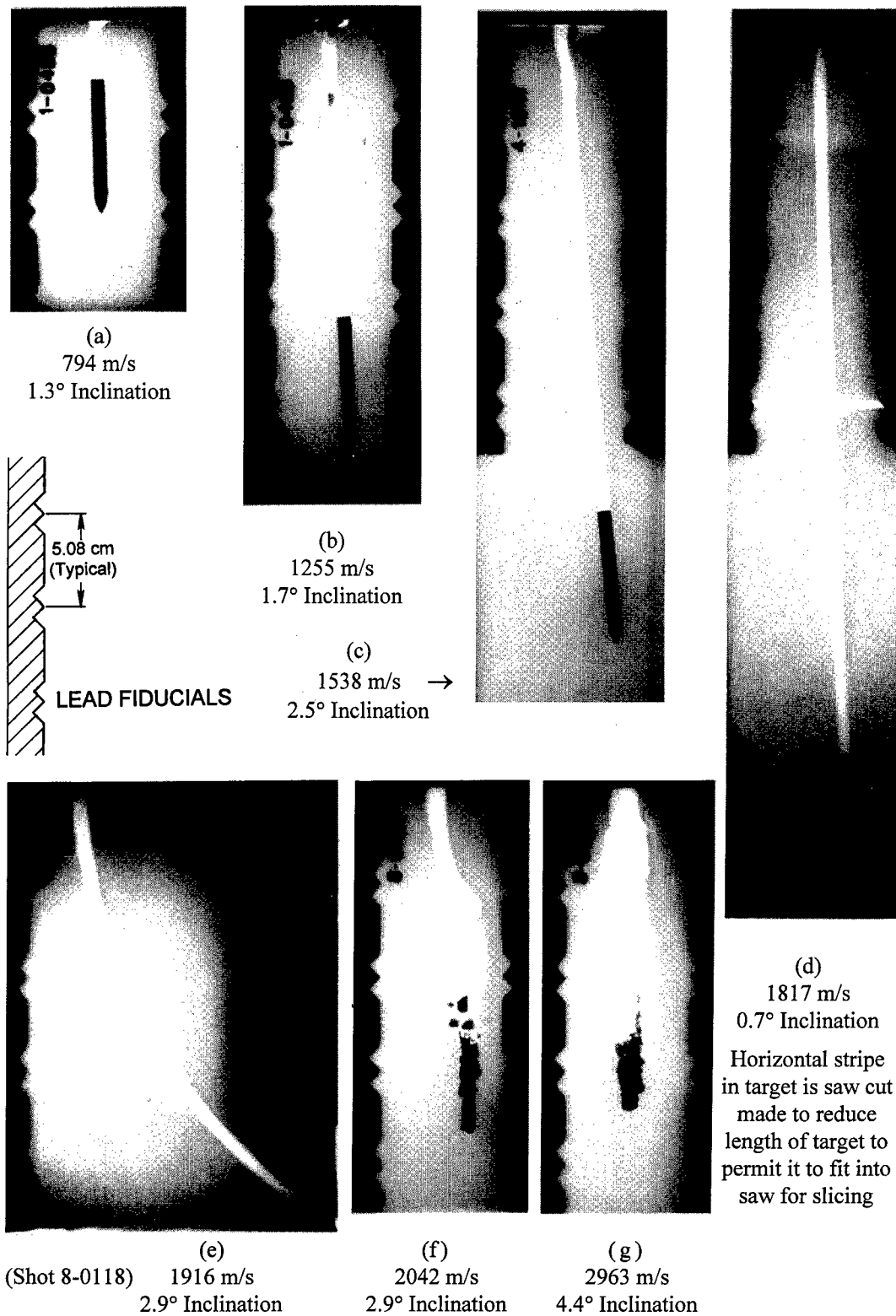


Fig. 3. Radiographs of craters produced by impact of ogive-nosed, AerMet 100 steel rods with 6061-T6511 aluminum targets. Striking velocity and the inclination angle of the rod at impact is noted below each crater.

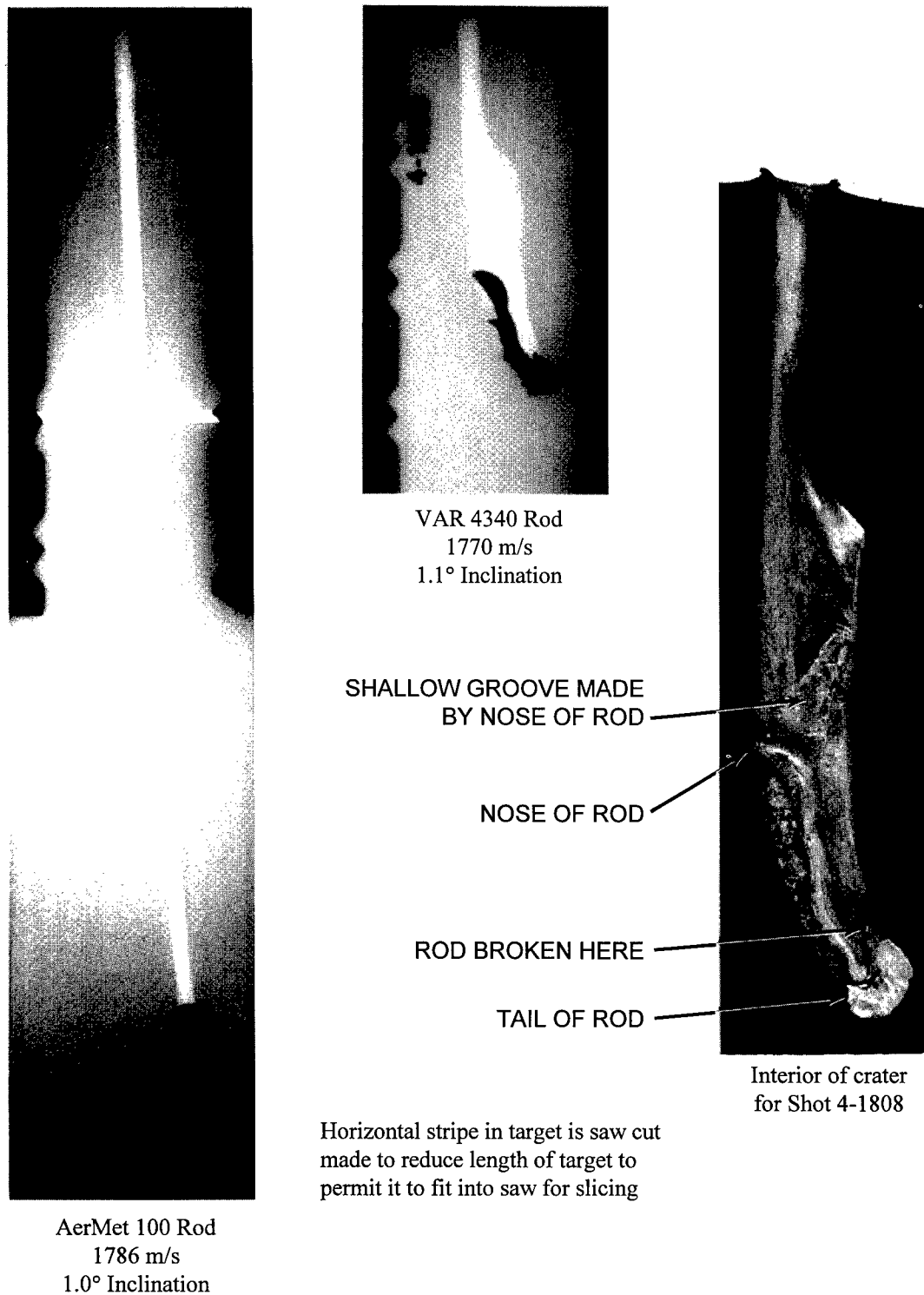


Fig. 4. Comparison of the crater produced by an AerMet 100 steel rod (left) with the crater produced by a VAR 4340 steel rod (center). Impact conditions for both tests were nearly identical and are noted below the craters. The crater for the VAR 4340 steel rod was cut open to examine the interior surfaces of the crater and the postimpact condition of the rod.

$$\begin{aligned} \frac{P}{(L+ka)} = & \left(\frac{\rho_p}{\rho_t} \right) \frac{1}{2CN} \left\{ \ln \left[1 + \frac{BN_1}{A} \left(\frac{V_s}{c_y} \right) + \frac{CN}{A} \left(\frac{V_s}{c_y} \right)^2 \right] \right\} \\ & + \left(\frac{\rho_p}{\rho_t} \right) \frac{BN_1}{CN(4ACN - B^2N_1^2)^{1/2}} \left\{ \tan^{-1} \left[\frac{BN_1}{(4ACN - B^2N_1^2)^{1/2}} \right] \right. \\ & \left. - \tan^{-1} \left[\frac{BN_1 + 2CN(V_s/c_y)}{(4ACN - B^2N_1^2)^{1/2}} \right] \right\} \end{aligned} \quad (1)$$

The projectile dimensioned in Fig. 1 has density ρ_p , shank length L , diameter $2a$, and caliber-radius-head ψ . The dimensionless parameters k , N , and N_1 are given by

$$k = (4\psi^2 - 4\psi/3 + 1/3)(4\psi - 1)^{1/2} - 4\psi^2(2\psi - 1) \sin^{-1} \left[\frac{(4\psi - 1)^{1/2}}{2\psi} \right] \quad (2a)$$

$$N = \frac{8\psi - 1}{24\psi^2} \quad (2b)$$

$$N_1 = \frac{(4\psi - 1)^{3/2}}{3\psi} + \frac{(2\psi - 1)^2(4\psi - 1)^{1/2}}{2\psi} - \psi(2\psi - 1)(\pi - 2\theta_0) \quad (2c)$$

$$\theta_0 = \sin^{-1} \left(\frac{2\psi - 1}{2\psi} \right) \quad (2d)$$

The target is described with density ρ_t and the dimensionless constants A , B , and C determined from the spherically symmetric, cavity-expansion analysis [7]. In addition, V_s is striking velocity and

$$c_y^2 = Y / \rho_t \quad (2e)$$

where Y is the quasi-static yield strength of the target [7].

Figure 5 compares our rigid, ogive-nose rod projectile model with the VAR 4340 steel and AerMet 100 steel projectile data given in Tables 1 and 2. We limit the data shown in Fig. 5 to striking velocities below 1.24 km/s for the VAR 4340 steel projectiles and 1.82 km/s for the AerMet 100 steel projectiles. Thus, we only present data in Fig. 5 for nondeforming projectiles. For input to the model, the target parameters are the same as those used or calculated in [7] and are given by $\rho_t = 2710 \text{ kg/m}^3$, $Y = 276 \text{ MPa}$, $A = 5.04$, $B = 0.983$, and $C = 0.940$. The projectiles dimensioned in Fig. 1 had $L = 59.3 \text{ mm}$, $l = 11.8 \text{ mm}$, $2a = 7.11 \text{ mm}$, and caliber-radius-head $\psi = 3.0$. The VAR 4340 steel density was 7830 kg/m^3 and the AerMet 100 density was 7890 kg/m^3 . In addition, the mass and Rockwell hardness of each projectile are given in Tables 1 and 2. As shown in Fig. 5, the rigid projectile model is in good agreement with model predictions.

If we define

$$\bar{P} = \frac{P}{L+l} \quad (3)$$

where \bar{P} is the penetration depth divided by the total rod length, the data in Fig. 5 cover the range, $0.82 < \bar{P} < 6.36$.

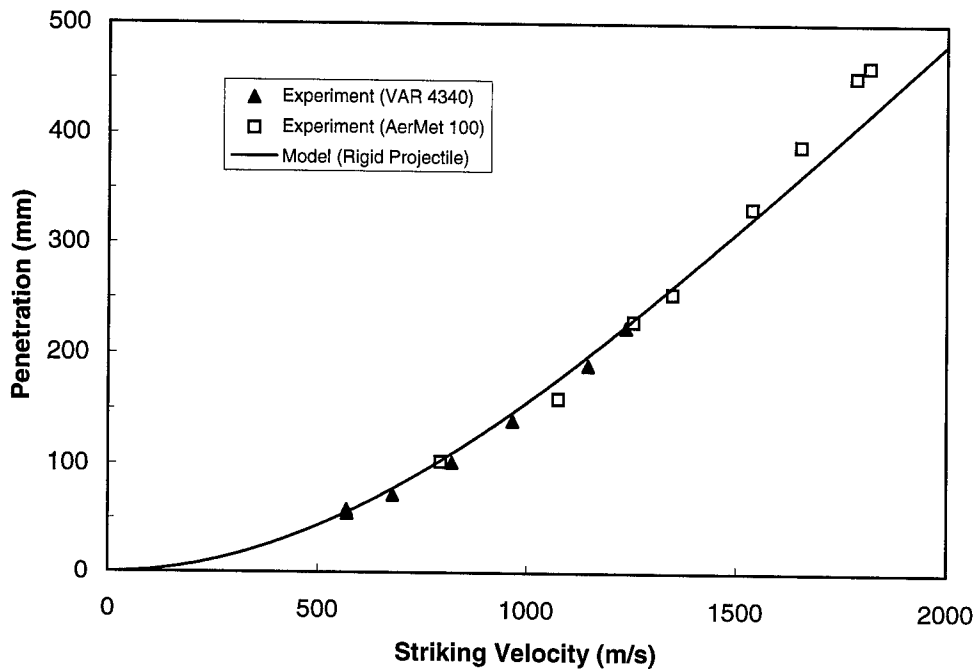


Fig. 5. Penetration depth versus striking velocity for the rigid-projectile response region.

BALLISTIC PERFORMANCE OF VAR 4340 AND AerMet 100 STEEL PROJECTILES

The penetration data given in Tables 1 and 2 for both projectile materials are shown in Fig. 6, along with a prediction from the rigid-projectile model. Not included in this figure are data from the experiments where the projectiles exited the side of the targets or for those tests in which the rod appeared to turn around. For Shots 4-1829 and 4-1799 in Table 1, the projectiles produced a curved penetration channel, so we used the curved path length for penetration depth P .

The data in Tables 1 and 2 and Fig. 6 show the regions of response as striking velocities increase. Response regions for the VAR 4340 steel projectiles include: (1) for $V_s < 1.24$ km/s, the projectiles remain visibly undeformed and the penetration channels are straight; (2) for $1.36 < V_s < 1.4$ km/s, the nose is visibly undeformed but the penetration channels are curved; (3) for $1.49 < V_s < 1.57$ km/s, the penetration channels are curved and the projectiles exited the side of the targets; (4) for $1.58 < V_s < 1.77$ km/s, the projectiles deformed severely and turned around in the targets; and (5) for $2.0 < V_s < 3.0$ km/s, the projectiles eroded and lost mass.

Response regions for the AerMet 100 steel projectiles include: (1) for $V_s < 1.82$ km/s, the projectiles remain visibly undeformed and the penetration channels are straight; (2) for $1.82 < V_s < 1.92$ km/s, the penetration channels were curved and the projectiles exited the sides of the target; (3) for $V_s \approx 2.0$ km/s, the front of the projectile broke into a number of large fragments and the rear of the rod remained intact (see Fig. 3f); and (4) for $V_s > 2.0$ km/s, the projectile fragment size decreased and the rod began to exhibit eroding-rod behavior and lose mass during penetration.

The response regions for both types of steel projectiles exhibit the same qualitative behavior as striking velocities increased. However, as mentioned previously, the AerMet 100 steel has about 1.5 times the tensile yield strength as the VAR 4340 steel for the heat treatment given the rods. Thus, the data presented in Tables 1 and 2 and Figs. 5 and 6 show an increase in projectile performance for the rigid-projectile response region for the AerMet 100 steel projectiles as compared with the VAR 4340 steel projectiles.

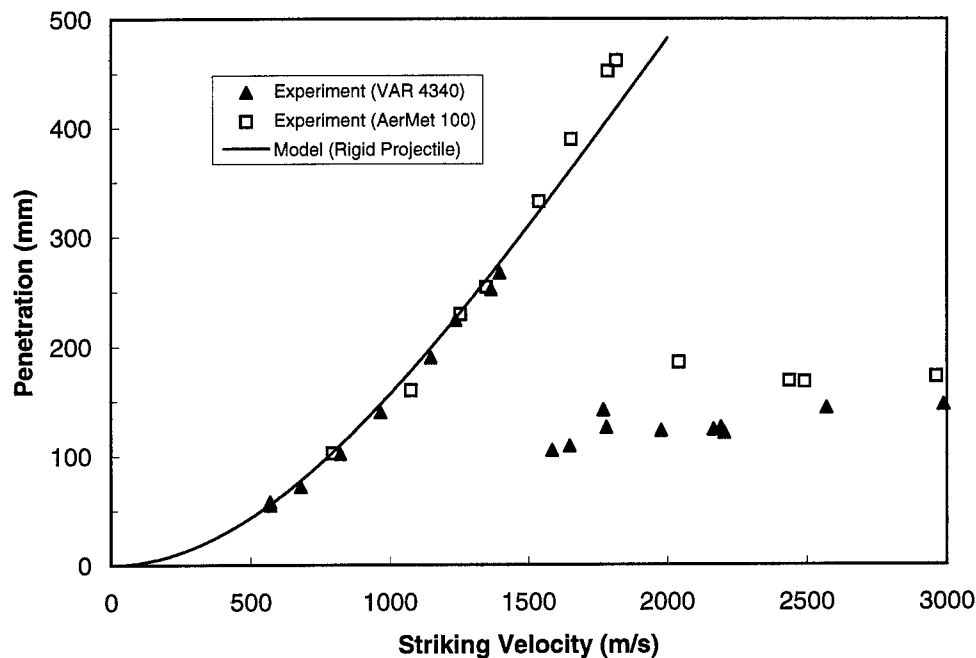


Fig. 6. Penetration depth versus striking velocity.

CONCLUSIONS

We conducted depth of penetration experiments with VAR 4340 (R_c 38) steel and AerMet 100 (R_c 53) steel, ogive-nose rod projectiles at striking velocities between 0.5 and 3.0 km/s. The various response regions for each steel projectile were identified and the ballistic performance of both steel materials was compared. In addition, we presented a rigid-projectile penetration model that accurately predicts the depth of penetration for striking velocities to 1.8 km/s.

Acknowledgment—This work was supported by the United States Department of Energy and the Joint DoD/DOE Munitions Technology Development Program. Sandia is a multiprogram laboratory operated by Sandia Corporation, a Lockheed Martin Company, for the United States Department of Energy under Contract DE-AC04-94AL85000.

REFERENCES

1. G. F. Silsby, Penetration of semi-infinite steel targets by rods at 1.3 to 4.5 km/s. *Proc. 8th Int. Symp. Ballistics*, TB/31-35, Orlando, FL (1984).
2. C. E. Anderson, S. A. Mullin, A. J. Piekutowski, N. W. Blaylock, and K. L. Poormon, Scale model experiments with ceramic laminate targets. *Int. J. Impact Engng* **18**, 1–22 (1996).
3. D. L. Orphal, R. R. Franzen, A. J. Piekutowski, and M. J. Forrestal, Penetration of confined aluminum nitride targets by tungsten long rods at 1.5–4.5 km/s. *Int. J. Impact Engng* **18**, 355–386 (1996).
4. *Data Bulletin—18 Percent Nickel Maraging Steels*, The International Nickel Company, Inc., New York, N.Y. 10005. (1964).
5. M. J. Forrestal, K. Okajima, and V. K. Luk, Penetration of 6061-T651 aluminum targets with rigid long rods. *J. Appl. Mech.*, **55**, 755–760 (1988).
6. M. J. Forrestal, V. K. Luk, Z. Rosenberg, and N. S. Brar, Penetration of 7075-T651 aluminum targets with ogival-nose rods. *Int. J. Solids Struct.* **29**, 1729–1736 (1992).
7. T. L. Warren and M. J. Forrestal, Effects of strain hardening and strain-rate sensitivity on the penetration of aluminum targets with spherical-nose rods. *Int. J. Solids Struct.*, **35**, 3737–3752 (1998).

8. W. F. Brown, H. Mindlin, and C.Y. Ho, *Aerospace Structural Metals Handbook*, Vol. 1, Code 1206, CINDAS/USAF CRDA Handbooks Operation, Purdue University, West Lafayette, IN 47907-1293, (1996).
9. *AerMet 100 Alloy, Alloy Steels 6*, Carpenter Technology Corporation, Carpenter Steel Division, Reading, PA 19612-4662, USA (1992).
10. J. Dahl, AerMet 100 – An advanced steel for the aerospace industry. *Advanced Materials Technology International*, 40–45 (1991).
11. M. J. Forrestal, D. Y. Tzou, E. Askari, and D. B. Longcope, Penetration into ductile metal targets with rigid spherical-nose rods. *Int. J. Impact Engng* **18**, 465–476 (1996).